JOURNAL OF COMPUTATIONAL PHYSICS **128,** 82–100 (1996)
ARTICLE NO. 0197

Comparison of Some Flux Corrected Transport and Total Variation Diminishing Numerical Schemes for Hydrodynamic and Magnetohydrodynamic Problems

GÁBOR TÓTH*,[1] AND DUŠAN ODSTRČIL†,[2]

*Sterrenkundig Instituut, Utrecht, The Netherlands; †Astronomical Institute, Ondřejov, Czech Republic

Received September 15, 1995; revised March 14, 1996

Two versions of flux corrected transport and two versions of total variation diminishing schemes are tested for several one- and two-dimensional hydrodynamic and magnetohydrodynamic problems. Two of the schemes, YDFCT and TVDLF are tested extensively for the first time. The results give an insight into the limitations of the methods, their relative strengths and weaknesses. Some subtle points of the algorithms and the effects of selecting different options for certain methods are emphasised.

1. INTRODUCTION

Many interesting and important problems arise in astrophysical, solar, magnetospheric, and thermonuclear research which can be described by the system of magnetohydrodynamic (MHD) equations. The complexity of these problems often prohibits an analytical investigation and/or only some of the variables can be observed or measured experimentally; thus the researcher has to rely on numerical simulations. In many situations, MHD flows develop steep gradients, shock waves, contact discontinuities, and shear layers that can be best resolved by modern high resolution schemes. Such schemes are well established for the modeling of hydrodynamic (HD) flows (see, e.g., Hirsch [1], LeVeque [2], or Fletcher [3]), but the extension of these schemes to the system of MHD equations has only recently begun by Ryu and Jones [4, 5], Balsara *et al.* [6], Dai and Woodward [7], Zachary *et al.* [8], and others referenced by them. The main reason for this delay is that the structure of the MHD equations is more complex than that of the HD equations, thus the relatively simple HD schemes become rather complicated and often need modifications to handle accurately the degeneracies and instabilities of the MHD equations. In our opinion, the complexity of some of the latest MHD schemes make their implementation prohibitively difficult for the nonspecialized researcher. In an effort to make the algorithms accurate, the flexibility and ease of modification or adaptability to specific problems are often compromised.

In this paper we take a rather pragmatic approach and test some of the simpler general methods on various numerical problems. Robustness, numerical diffusivity, production of spurious oscillations and computational efficiency are all taken into account; thus we hope to gain some balanced view on the properties of different schemes in different situations.

The basic concept behind all high-resolution numerical schemes is to use a high-order scheme as much as possible and in the meantime to add intelligently sufficient dissipation in the localized steep gradient regions to eliminate possible numerical oscillations. It is this adaptive dissipation property that distinguishes the modern and classical numerical schemes. An early attempt toward developing high-order monotonic schemes was made by Boris and Book [9], who proposed the flux-corrected transport (FCT) techniques. This procedure adds high-order (''anti-diffusive'') terms to the stable but diffusive low-order solution and a limiter ensures that no new minima or maxima with respect to the low-order solution are created. The concept of total variation diminishing (TVD) schemes was introduced by Harten [10]. For certain types of equations these algorithms can ensure that the total variation of the flow variables does not increase with time; thus no spurious numerical oscillations are generated. The solution can be second- or third-order accurate in the smooth parts of the solution, but the scheme ''switches'' to first order at extrema. TVD schemes are often based on approximate or exact Riemann solvers, but, as Yee [11] observed, a high-order TVD Lax–Friedrichs (TVDLF) scheme can be formulated without using any Riemann solver. Although the simplicity of the TVDLF formulation is very appealing, it seems to have received little attention (Cockburn *et al.* [12]) especially in the context of MHD problems (Barmin et al. [13]). The more accurate, but more complex, TVD scheme with the local characteristics approach (Yee [11]) will serve as a basis for comparison.

It is important to note that the monotonicity of the FCT

[1] E-mail: toth@fys.ruu.nl.
[2] E-mail: odstrcil@asu.cas.cz.

0021-9991/96 $18.00

algorithm or the TVD property of the TVD schemes has never been proved for a system of nonlinear equations, like the MHD equations; thus for MHD problems the desired features of the schemes have to be confirmed by numerical tests. This fact also prompts a rather humble approach when we modify the schemes; only numerical tests can tell if a modification improves performance or not. Mathematical proofs for simplified equations can only provide hints. It is also an open question how well the essentially one-dimensional schemes will perform in multidimensional simulations. Besides monotonicity and the conservation of mass, momentum, and energy, one may require the scheme to satisfy other criteria; certain quantities like density and pressure should remain positive under all circumstances, or a particular function of the variables (e.g., the divergence of the magnetic field) should be conserved.

Comparison of numerical schemes has a long tradition. Woodward and Colella's [14] seminal paper on HD problems with shocks still provides a guideline in the choice of numerical schemes for hydrodynamical simulations. Such an extensive study (with several algorithms) for MHD flows with discontinuities has not been published yet to the best of our knowledge. (Stone *et al.* [15] published a test suite with results produced by the Zeus code), so we set out to evaluate some FCT and TVD numerical schemes for a rather large set of HD and ideal MHD test problems.

In Section 2 the system of time-dependent ideal MHD equations are discussed. Numerical schemes based on the flux-corrected transport and the total variation diminishing techniques are described in Section 3. Section 4 compares the performance of the different numerical schemes for the basic advection tests and for some one- and two-dimensional HD and MHD problems. Finally, in Section 5 we summarize our experience with different numerical schemes and provide suggestions for their application, as well as directions for further work.

2. MATHEMATICAL DESCRIPTION

The numerical schemes investigated in this paper were designed to explicitly solve a set of conservation laws. Nonstiff source terms can be included by temporal splitting or in an unsplit fashion, but here we shall concentrate on homogeneous equations. The ideal MHD equations provide a complex yet important example. The plasma is described by the primitive variables V, i.e., the mass density ρ, velocity $\mathbf{v}$, pressure p, and magnetic field $\mathbf{B}$, which are all functions of time t and three (if no simplifying symmetry assumption is made) spatial coordinates $\mathbf{x}$. The MHD equations can be expressed in various mathematical forms. However, for numerical models the conservative form is often preferred; the equations explicitly represent the conservation of mass, momentum, total energy, and induction of the magnetic field. The conservative variables U are ρ, the momentum density $\rho\mathbf{v}$, the total energy density e, and $\mathbf{B}$. The conservative system of ideal MHD equations is

$$\frac{\partial}{\partial t}(\rho) + \nabla\cdot(\rho\mathbf{v}) = 0, \tag{1}$$

$$\frac{\partial}{\partial t}(\rho\mathbf{v}) + \nabla\cdot(\rho\mathbf{v}\mathbf{v}) = -\nabla p_{\text{tot}} + \nabla\cdot\left(\frac{\mathbf{B}\mathbf{B}}{\mu}\right) - (\nabla\cdot\mathbf{B})\frac{\mathbf{B}}{\mu}, \tag{2}$$

$$\frac{\partial}{\partial t}(e) + \nabla\cdot(e\mathbf{v}) = -\nabla\cdot(p_{\text{tot}}\mathbf{v}) + \nabla\cdot\left(\frac{\mathbf{B}\mathbf{B}\cdot\mathbf{v}}{\mu}\right) - (\nabla\cdot\mathbf{B})\frac{\mathbf{B}\cdot\mathbf{v}}{\mu}, \tag{3}$$

$$\frac{\partial}{\partial t}(\mathbf{B}) + \nabla\cdot(\mathbf{v}\mathbf{B}) = \nabla\cdot(\mathbf{B}\mathbf{v}) - (\nabla\cdot\mathbf{B})\mathbf{v}, \tag{4}$$

where $\nabla\cdot(\mathbf{B}\mathbf{v})_j = \sum_i \partial(B_i v_j)/\partial x_i$ in Cartesian coordinates. The initial conditions have to satisfy

$$\nabla\cdot\mathbf{B} = 0. \tag{5}$$

The exact solution of the MHD equations (1)–(4) keeps $\nabla\cdot\mathbf{B} = 0$ indefinitely; thus the expressions proportional to $\nabla\cdot\mathbf{B}$, the rightmost terms in (2)–(4), are zero analytically. However, in multidimensional simulations numerical errors may lead to a finite divergence of the magnetic field. Powell [29] discovered that including these corrective terms and the corresponding characteristic *divergence wave*, can stabilize the solution of Riemann-solver based algorithms. We found that using the corrective terms in multidimensional calculations improved the solution for the FCT and TVDLF schemes as well. It should be noted that the terms are nonconservative; thus conservation of momentum, energy, and magnetic flux are not strictly enforced any longer. For one-dimensional problems $\nabla\cdot\mathbf{B} = 0$ is equivalent with $\partial B_x/\partial t = 0$, which is satisfied exactly and trivially with or without Powell's corrective terms.

In Eqs. (2) and (3) the total pressure,

$$p_{\text{tot}} = p + \frac{\mathbf{B}^2}{2\mu}, \tag{6}$$

is a sum of the thermal and magnetic pressures. In the conservative formulation the thermal pressure is determined from the total energy density,

$$e = \frac{p}{\gamma - 1} + \frac{\rho\mathbf{v}^2}{2} + \frac{\mathbf{B}^2}{2\mu}, \tag{7}$$

which is a sum of thermal, kinetic, and magnetic energy

densities. Here we assumed an ideal gas with an adiabatic index γ, but note that a more general equation of state can be easily incorporated into the FCT and TVDLF schemes, while it causes substantial complications for Riemann solver-based algorithms. In the rest of the paper we use units where the magnetic permeability $\mu = 1$. By setting $\boldsymbol{B} = 0$ we retain the equations of compressible HD.

In explicit integration schemes the time step is restricted by the Courant–Friedrichs–Levy (CFL) condition,

$$\Delta t \le C \min_{q=x,y,z} \left(\frac{\Delta q}{c_q^{\max}} \right), \tag{8}$$

where C is the Courant number and $c_q^{\max}$ is the maximum propagation speed of information in direction q. For the hyperbolic system of ideal MHD equations this speed is

$$c_q^{\max} = |v_q| + c_q^f = |v_q| + \frac{1}{\sqrt{2}} \left[\frac{\gamma p + \mathbf{B}^2}{\rho} + \sqrt{\left(\frac{\gamma p + \mathbf{B}^2}{\rho} \right)^2 - 4 \frac{\gamma p B_q^2}{\rho^2}} \right]^{1/2}, \tag{9}$$

where c_q^f is the speed of the fast-mode MHD wave, relative to the fluid in the $q = x, y, z$ directions.

3. NUMERICAL SCHEMES

Here we provide a self-contained description of some FCT and TVD algorithms in one dimension on a stationary uniform grid with the space variable denoted by x. We repeat and recast the definitions to clarify some important points and to facilitate comparison of the algorithms.

For FCT on nonuniform or moving grids see Boris [16]. Yee *et al.* [17] describes TVD schemes with generalized coordinates, and another finite volume formulation is given by Wang and Widhopf [19]. A fully multidimensional FCT scheme is described by Zalesak [20], and DeVore [21] extends it to staggered grids to keep the $\nabla \cdot \mathbf{B} = 0$ condition to roundoff errors. A fully multidimensional TVD MacCormack scheme can be found in Yee's [11] paper.

The easiest way to generalize a one-dimensional scheme to multidimensional problems is via a Strang-type [22] operator splitting, e.g., in two dimensions,

$$U^{n+1} = L_x^{\Delta t/2} L_y^{\Delta t} L_x^{\Delta t/2} U^n, \tag{10}$$

where L_x and L_y are the appropriate one-dimensional operators for a given time step with spatial derivatives taken in the x and y directions, respectively. A somewhat faster and usually satisfactory method is alternating the order of L_x and L_y with every time step; thus

$$U^{n+2} = L_x L_y U^{n+1} = L_x L_y L_y L_x U^n. \tag{11}$$

In all the two-dimensional tests we took this latter approach.

In the following descriptions the value of the discretised conservative variable U_j^n is defined on the mesh at the discrete time level t^n as a volume average within the jth mesh-cell centered at position x_j. The cell interfaces are at $x_{j-1/2}$ and $x_{j+1/2}$, where $x_{j+1/2} = (x_j + x_{j+1})/2$. We shall also use the notation $\Delta U_{j+1/2} = U_{j+1} - U_j$ for the difference of variables in adjacent cells. The subscript $j + 1/2$ will always refer to a quantity centered on the cell interface at $x_{j+1/2}$, while a time-centered quantity will be denoted by a superscript $n + 1/2$.

3.1. *Flux-Corrected-Transport (FCT) Algorithms*

The FCT scheme solves the equations for each conservative variable separately. The algorithm discretises the transport flux $f = \mathbf{v}U$ and the rest of the spatial derivatives S (the right-hand sides of Eqs. (1)–(4), in FCT terminology the "source terms") slightly differently. The solution is advanced from time level n to $n + 1$ in two steps:

the half step,

$$U_j^t = U_j^n - \frac{\Delta t}{2\Delta x} (f_{j+1/2}^n - f_{j-1/2}^n) + \frac{\Delta t}{2} S_j^n \tag{12}$$

$$U_j^d = U_j^t + D_{j+1/2}^n - D_{j-1/2}^n \tag{13}$$

$$U_j^{n+1/2} = U_j^d - \tilde{A}_{j+1/2}^n + \tilde{A}_{j-1/2}^n; \tag{14}$$

the full step,

$$U_j^T = U_j^n - \frac{\Delta t}{\Delta x} (f_{j+1/2}^{n+1/2} - f_{j-1/2}^{n+1/2}) + \Delta t S_j^{n+1/2} \tag{15}$$

$$U_j^D = U_j^T + D_{j+1/2}^{n+1/2} - D_{j-1/2}^{n+1/2} \tag{16}$$

$$U_j^{n+1} = U_j^D - \tilde{A}_{j+1/2}^{n+1/2} + \tilde{A}_{j-1/2}^{n+1/2}, \tag{17}$$

where D is the diffusive flux which introduces a numerical diffusion to the solution in order to ensure stability and monotonicity and $\tilde{A}$ is the corrected anti-diffusive flux which eliminates the excessive numerical diffusion where it is possible. The superscripts t and d refer to the "transport" and "diffusion" stages respectively at the half step, while T and D refer to the respective stages at the full step. The usage of fluxes at cell interfaces ensures the conservation property, because the same quantities are added as input for one cell and subtracted as output for an adjacent cell.

The transport fluxes are

$$f_{j+1/2}^n = U_{j+1/2}^n v_{j+1/2}^n, \quad f_{j+1/2}^{n+1/2} = U_{j+1/2}^n v_{j+1/2}^{n+1/2}, \tag{18}$$

where $U_{j+1/2} = (U_{j+1} + U_j)/2$ and $v_{j+1/2} = (v_{j+1} + v_j)/2$. Note that U^n is used to compute the time-centered transport flux $f^{n+1/2}$. In contrast, the $S^{n+1/2}$ "sources" are fully time centered; e.g., the gradient of total pressure in the momentum equation (2) is discretised as

$$S_j^{n+1/2} = \frac{1}{2\Delta x}\,[p_{\mathrm{tot}}(U_{j+1}^{n+1/2}) - p_{\mathrm{tot}}(U_{j-1}^{n+1/2})], \qquad (19)$$

which is identical to centering the sources on the cell interfaces. Alternatively one can center the conservative variables

$$S_j^{n+1/2} = \frac{1}{\Delta x}\,[p_{\mathrm{tot}}(U_{j+1/2}^{n+1/2}) - p_{\mathrm{tot}}(U_{j-1/2}^{n+1/2})], \qquad (20)$$

or the primitive variables

$$S_j^{n+1/2} = \frac{1}{\Delta x}\,[p_{\mathrm{tot}}(V_{j+1/2}^{n+1/2}) - p_{\mathrm{tot}}(V_{j-1/2}^{n+1/2})]. \qquad (21)$$

In the FCT calculations performed in this paper we use the first centering, although we found that centering the primitive variables leads to comparable results. We note that the spatial centering of the transport flux should always use the original prescription Eq. (18) to avoid adverse effects in some cases, like in the problem of strong rarefaction waves in Section 4.4.

The diffusive fluxes are

$$D_{j+1/2}^n = \nu_{j+1/2}^n\,\Delta U_{j+1/2}^n, \quad D_{j+1/2}^{n+1/2} = \nu_{j+1/2}^{n+1/2}\,\Delta U_{j+1/2}^n, \qquad (22)$$

where the diffusion coefficients $\nu_{j+1/2}$ will be specified in the following two subsections. Again, U^n is used to compute the time-centered diffusive flux $D^{n+1/2}$.

The amount of the anti-diffusive flux is controlled by a limiter to avoid the formation of new maxima or minima with respect to the transported and diffused solution,

$$\tilde{A}_{j+1/2}^n = s_{j+1/2}^n \max[0, \min(|A_{j+1/2}^n|, s_{j+1/2}^n\,\Delta U_{j-1/2}^d, s_{j+1/2}^n\,\Delta U_{j+3/2}^d)] \qquad (23)$$

$$\tilde{A}_{j+1/2}^{n+1/2} = s_{j+1/2}^{n+1/2} \max[0, \min(|A_{j+1/2}^{n+1/2}|, s_{j+1/2}^{n+1/2}\,\Delta U_{j-1/2}^D, s_{j+1/2}^{n+1/2}\,\Delta U_{j+3/2}^D)] \qquad (24)$$

where $s_{j+1/2}^n = \mathrm{sgn}(\Delta U_{j+1/2}^d)$ and $s_{j+1/2}^{n+1/2} = \mathrm{sgn}(\Delta U_{j+1/2}^D)$. The uncorrected anti-diffusive flux $A_{j+1/2}$ will be specified in the following subsections.

A more general limiter, especially suitable for explicitly multidimensional implementations with no dimensional splitting, is described by Zalesak [20].

3.2. *ETBFCT*

In ETBFCT (Boris [16], the meaning of ETB is *probably* explicitly treated boundary) the uncorrected anti-diffusive fluxes are

$$A_{j+1/2}^n = \mu_{j+1/2}^n\,\Delta U_{j+1/2}^t, \quad A_{j+1/2}^{n+1/2} = \mu_{j+1/2}^{n+1/2}\,\Delta U_{j+1/2}^T \qquad (25)$$

with the diffusion and anti-diffusion coefficients

$$\begin{aligned} \nu_{j+1/2}^n &= \tfrac{1}{6} + \tfrac{1}{3}\,(\varepsilon_{j+1/2}^n)^2, \quad \mu_{j+1/2}^n = \tfrac{1}{6} - \tfrac{1}{6}\,(\varepsilon_{j+1/2}^n)^2 \\ \nu_{j+1/2}^{n+1/2} &= \tfrac{1}{6} + \tfrac{1}{3}\,(\varepsilon_{j+1/2}^{n+1/2})^2, \quad \mu_{j+1/2}^{n+1/2} = \tfrac{1}{6} - \tfrac{1}{6}\,(\varepsilon_{j+1/2}^{n+1/2})^2, \end{aligned} \qquad (26)$$

where

$$\varepsilon_{j+1/2}^n = \frac{1}{2}\,\frac{\Delta t}{\Delta x}\,v_{j+1/2}^n, \quad \varepsilon_{j+1/2}^{n+1/2} = \frac{\Delta t}{\Delta x}\,v_{j+1/2}^{n+1/2}. \qquad (27)$$

With these definitions $A = D$ when the velocity and the S "sources" are zero; thus there is no "residual" diffusion as in the original SHASTA scheme by Boris and Book [9]. When the velocity is nonzero, the ε^2 terms reduce the amplitude and phase errors to fourth order for linear convection problems.

ETBFCT should be used with $\varepsilon^{n+1/2} \le 0.5$ everywhere to ensure the monotonicity at steep gradients; thus setting the Courant number $C \le 0.5$ in Eq. (8) is recommended.

3.3. *YDFCT*

Odstrčil [23] noted that the transported values U^T are not the only ones which remain unchanged by the difference scheme when f and S are zero. "Phoenical" anti-diffusive fluxes can also be obtained using the half-step values $U^{n+1/2}$ at the full step. In YDFCT (the YD is just a notation used to distinguish the different experimental versions of the scheme) the uncorrected anti-diffusive flux in the full step is modified to

$$A_{j+1/2}^{n+1/2} = \mu_{j+1/2}^{n+1/2}\ \max(|\Delta U_{j+1/2}^{n+1/2}|, \tfrac{1}{2}\,|\Delta U_{j+1/2}^T|) \qquad (28)$$

which eliminates the edge erosion problem as described by Odstrčil [24].

In YDFCT the diffusive fluxes are split in order to reach higher phase accuracy; thus the half-step transport in Eq. (12) is redefined as

$$\begin{aligned} U_j^t = U_j^n - \frac{\Delta t}{2\Delta x}\,(f_{j+1/2}^n - f_{j-1/2}^n) + \frac{\Delta t}{2}\,S_j^n \\ + (\gamma_{j+1/2}^n\,\Delta U_{j+1/2}^n - \gamma_{j-1/2}^n\,\Delta U_{j-1/2}^n) \end{aligned} \qquad (29)$$

with

$$\gamma_{j+1/2}^n = \tfrac{1}{60} + \tfrac{1}{60}\,(\varepsilon_{j+1/2}^n)^2. \qquad (30)$$

Finally, the full-step diffusion and anti-diffusion coefficients are also modified,

$$\nu_{j+1/2}^{n+1/2} = \tfrac{1}{3} + \tfrac{1}{6}(\varepsilon_{j+1/2}^{n+1/2})^2, \quad \mu_{j+1/2}^{n+1/2} = \tfrac{1}{3} - \tfrac{1}{3}(\varepsilon_{j+1/2}^{n+1/2})^2, \qquad (31)$$

enabling YDFCT to use time steps that are twice as large as those that ETBFCT can, because the monotonicity property is ensured for $\varepsilon^{n+1/2} \le 1$. We note that the increased diffusion and anti-diffusion coefficients exclude a fully multidimensional implementation of YDFCT, because there the sum of the diffusion coefficients for the two or three spatial directions exceeds $\frac{1}{2}$ and a numerical instability (independent of the time step) results. ETBFCT may have similar problems in unsplit three-dimensional computations. On the other hand, for dimensionally split implementations YDFCT seems to be superior to ETBFCT.

3.4. *Total Variation Diminishing (TVD) Algorithms*

The total variation diminishing (TVD) schemes ensure that the total variation does not increase with time

$$\sum_j |\Delta U_{j+1/2}^{n+1}| \le \sum_j |\Delta U_{j+1/2}^{n}|. \qquad (32)$$

In contrast with FCT, all spatial derivatives in a conservation form are included in the F fluxes of TVD, i.e., $F = f - S$, and the equations are solved simultaneously. Thus U and F are vectors of the conservative variables and their respective flux functions. The contribution of terms in nonconservative form, e.g., physical source terms, or Powell's corrective sources, are added separately without the limiting procedures of TVD. The characteristic based TVD schemes also use the c^k eigenvalues and the r^k right and l^k left eigenvectors of the $\partial F/\partial U$ matrix. Following Yee [11], we define a rather large class of TVD schemes and then select a few special cases for our tests.

In the non-MUSCL class of TVD schemes the interface fluxes are simple averages of the cell-centered fluxes; thus

$$U_j^T = U_j^n - \frac{\Delta t}{2\Delta x}(F_{j+1}^n - F_{j-1}^n) \qquad (33)$$

$$U_j^{n+1} = U_j^T + \tfrac{1}{2}(\Phi_{j+1/2} - \Phi_{j-1/2}). \qquad (34)$$

The limiter $\Phi_{j+1/2}$ is a function of some symmetric average $U_{j+1/2}$ of U_j^n and U_{j+1}^n (e.g., the arithmetic mean, or the Roe [25] average for hydrodynamics, or it is calculated from the arithmetic mean of the primitive variables $[V_j^n + V_{j+1}^n]/2$) and of their difference $\Delta U_{j+1/2}$. Second-order accuracy in time is achieved by a second-order correction term included in Φ (see in Eq. (49)). Alternatively, the first-order U^T can be replaced by some second-order approximation (e.g., MacCormack-type), in which case Φ should not include the correction term. The MacCormack formulation allows for second-order accurate (in time) unsplit source terms and can also be made fully multidimensional with no dimensional splitting.

The MUSCL (monotonic upwind schemes for conservation laws) TVD schemes achieve the second-order temporal accuracy by the Hancock predictor step,

$$U_j^{n+1/2} = U_j^n - \frac{1}{2}\frac{\Delta t}{\Delta x}[F(U_j^n + \tfrac{1}{2}\overline{\Delta U}_j^n) - F(U_j^n - \tfrac{1}{2}\overline{\Delta U}_j^n)], \qquad (35)$$

where the limited differences $\overline{\Delta U}^n$ will be defined in Section 3.7. In the full step upwinded left and right states, denoted by U^{L} and U^{R}, are formed from $U^{n+1/2}$,

$$U_{j+1/2}^L = U_j^{n+1/2} + \tfrac{1}{2}\overline{\Delta U}_j^n, \quad U_{j+1/2}^R = U_{j+1}^{n+1/2} - \tfrac{1}{2}\overline{\Delta U}_{j+1}^n, \qquad (36)$$

and the flux at the cell interface is calculated as $F^{\mathrm{LR}} = [F(U^{\mathrm{L}}) + F(U^{\mathrm{R}})]/2$. The dissipative limiter Φ^{LR} is a function of some symmetric average U^{LR} of U^{R} and U^{L}, and of the difference $\Delta U^{\mathrm{LR}} = U^{\mathrm{R}} - U^{\mathrm{L}}$. With these definitions the full step is

$$U_j^T = U_j^n - \frac{\Delta t}{\Delta x}(F_{j+1/2}^{\mathrm{LR}} - F_{j-1/2}^{\mathrm{LR}}) \qquad (37)$$

$$U_j^{n+1} = U_j^T + \tfrac{1}{2}(\Phi_{j+1/2}^{\mathrm{LR}} - \Phi_{j-1/2}^{\mathrm{LR}}). \qquad (38)$$

Unlike in FCT, the "transport stage" U^T is used in (34) and (38) only; thus F and Φ could be combined in a single modified flux. Note that the limited differences are always calculated from U^n and not from $U^{n+1/2}$. The latter choice leads to severe degradation of results even for the simple convection tests. We also note that the Hancock predictor is superior to a simple Euler transport step. These observations warn against the use of the simplifications proposed by Barmin et al. [13].

3.5. *TVD Lax–Friedrichs Scheme*

There are many TVD schemes. However, we are interested in Yee's [11] high order Lax–Friedrichs TVD scheme because it does not use a Riemann solver; thus it can be applied to any system of conservation laws without knowledge of the characteristic waves. Yee originally defined $\Phi_{j+1/2}^{\mathrm{LR}} = \Phi_{j+1/2}^{\mathrm{Yee}} = \Delta U_{j+1/2}^{\mathrm{LR}}$, but this leads to a very diffusive scheme. It is also suspect to a pair-wise coupling of the cells if the initial conditions are such, in which case the method reduces to the even more diffusive first-order Lax–Friedrichs scheme. If we multiply Φ^{Yee} by the global or the local Courant number the diffusion is reduced (and the coupling problem is also eliminated) and, according to

the numerical tests, the scheme preserves most of the desired properties of a TVD scheme:

$$\Phi^{\mathrm{TVDLF}}_{j+1/2} = \frac{\Delta t}{\Delta x} c^{\max}_{j+1/2} \Delta U^{\mathrm{LR}}_{j+1/2}. \tag{39}$$

Cockburn *et al.* [12] take $c^{\max}_{j+1/2} = \max[c^{\max}_x(U^{\mathrm{R}}), c^{\max}_x(U^{\mathrm{L}})]$, while Barmin *et al.* [13] use $c^{\max}_{j+1/2} = c^{\max}_x(U^{\mathrm{LR}})$, where $c^{\max}_x$ has been defined in Eq. (9) for the MHD equations. We take the latter since it is computationally less expensive, and it is consistent with the Riemann-solver-type TVD schemes, where the eigenvectors and eigenvalues are also evaluated at the averaged U^{LR}. We tried to further reduce $c^{\max}$ for some of the conserved variables, e.g., using $|v_x|$ for density, or the Alfvén speed $|B_x|/\sqrt{\rho}$ for the magnetic field, but some spurious oscillations were observed with no significant improvement in the resolution of discontinuities.

3.6. *TVD with Local Characteristics Approach*

As a basis of comparison for the simple FCT and TVDLF methods, we implemented (Tóth [26, 27]) some TVD schemes based on an approximate Riemann solver following Yee's [11] local characteristics approach. The eigenvectors for the MHD equations were taken from Roe and Balsara [28]. Powell's [29] extension of the 7×7 eigensystem to an eight-wave Riemann solver is also implemented (see Gombosi *et al.* [30]) to stabilize the TVD scheme against instabilities related to numerical errors in maintaining $\nabla \cdot \mathbf{B} = 0$. The eight-wave Riemann solver advects the errors in $\nabla \cdot \mathbf{B}$ away, but it does not eliminate them. Since a major part of Yee's work has been published in technical memoranda, we feel it is useful to repeat the definitions in a concise and uniform way while an effort is made to remove the typos of previous publications.

The jump in the kth characteristic wave

$$\alpha^k_{j+1/2} = l^k_{j+1/2} \cdot \Delta U_{j+1/2} \tag{40}$$

is the scalar product of $\Delta U_{j+1/2}$ and the kth column l^k of the left eigenvector matrix $L = R^{-1}$ evaluated at $U_{j+1/2}$. The corresponding eigenvalue $c^k_{j+1/2}$ is also calculated from $U_{j+1/2}$, and it is made dimensionless:

$$a^k_{j+1/2} = \frac{\Delta t}{\Delta x} c^k_{j+1/2}. \tag{41}$$

Now the ϕ limiter for the kth characteristic field can be any of the following expressions in the non-MUSCL formulation,

$$\phi^{\mathrm{Harten}}_{j+1/2} = \alpha_{j+1/2}(|a^*| - a^2)_{j+1/2} - \tfrac{1}{2}\left[\overline{\alpha(|a| - a^2)}_j + \overline{\alpha(|a| - a^2)}_{j+1}\right] \tag{42}$$

$$\phi^{\mathrm{Yee}}_{j+1/2} = \alpha_{j+1/2}(|a^*| - a^2)_{j+1/2} - \tfrac{1}{2}(\overline{\alpha}_j + \overline{\alpha}_{j+1})(|a| - a^2)_{j+1/2} \tag{43}$$

$$\phi^{\mathrm{Sweby}}_{j+1/2} = \alpha_{j+1/2}(|a| - a^2)_{j+1/2} - \overline{\alpha(|a| - a^2)}_{j+\sigma} \tag{44}$$

$$\phi^{\mathrm{Roe}}_{j+1/2} = (\alpha_{j+1/2} - \overline{\alpha}_{j+\sigma})(|a| - a^2)_{j+1/2}, \tag{45}$$

where the k superscripts were dropped and in the Sweby and Roe limiters $\sigma = 1$ for $a_{j+1/2} < 0$ and 0 otherwise. In the Harten limiter

$$a^*_{j+1/2} = a_{j+1/2} + \frac{\overline{\alpha(|a| - a^2)}_{j+1} - \overline{\alpha(|a| - a^2)}_j}{2\alpha_{j+1/2}} \tag{46}$$

while in Yee's modified version

$$a^*_{j+1/2} = a_{j+1/2} + \frac{\overline{\alpha}_{j+1} - \overline{\alpha}_j}{2\alpha_{j+1/2}} (|a| - a^2)_{j+1/2} \tag{47}$$

and $a^* = a$, where $\alpha_{j+1/2} = 0$. Harten's artificial compression term is not included here; on the other hand, we allow sharper slope limiters than the original minmod limiter (see Section 3.7).

Although it may not be apparent, $\phi^{\mathrm{Yee}} = \phi^{\mathrm{Roe}}$ and $\phi^{\mathrm{Harten}} = \phi^{\mathrm{Sweby}}$ unless an entropy fix is applied, which simply means that $|a|$ in Eqs. (42)–(47) should be replaced everywhere by

$$\psi(a) = \begin{cases} |a|, & \text{if } |a| \geq \delta_k, \\ (a^2 + \delta_k^2)/2\delta_k, & \text{otherwise,} \end{cases} \tag{48}$$

and, similarly, $|a^*|$ should be replaced by $\psi(a^*)$. Here δ_k is some small parameter for the kth characteristic field. Ryu and Jones [4] take 0.2 for the fast and slow waves, 0.4 for the Alfvén waves, and 0 for the entropy wave. There are other types of entropy fixes in the literature, but their evaluation is beyond the scope of this paper. The entropy fix is not applied in the simulations shown in this paper, and the $\phi^{\mathrm{Yee}} = \phi^{\mathrm{Roe}}$ limiter is used.

When the predictor step in Eq. (33) is only first-order accurate in time, a second-order correction is added,

$$\phi^*_{j+1/2} = \phi_{j+1/2} + a^2_{j+1/2}\alpha_{j+1/2}. \tag{49}$$

Finally, the characteristic limiter ϕ^* (or ϕ for a second-order predictor, instead of Eq. (33)) is transformed back to the limiter Φ in Eq. (34) for the conservative variables U,

$$\Phi = \sum_k r^k \phi^{*k}, \tag{50}$$

where r^k is the kth eigenvector in the right eigensystem-matrix R.

For the MUSCL approach the limiting has already been applied to the arguments of $\phi^{\mathrm{LR}}(U^{\mathrm{L}}, U^{\mathrm{R}})$; thus we simply have (cf. (42)—(45))

$$\phi^{\mathrm{LR}}_{j+1/2} = \alpha^{\mathrm{LR}}_{j+1/2}\psi(a^{\mathrm{LR}}_{j+1/2}), \tag{51}$$

where α^{LR} and a^{LR} are defined by (40) and (41) with $U_{j+1/2}$ and $\Delta U_{j+1/2}$ replaced by $U^{\mathrm{LR}}_{j+1/2}$ and $\Delta U^{\mathrm{LR}}_{j+1/2}$, respectively.

It is now quite clear how the TVDLF method is derived. Replacing $\psi(a^k)$ by $|a^{\max}| = c^{\max}\,\Delta t/\Delta x$ will increase the diffusion, but it removes the dependence on the k index of the characteristic variables. In the case of TVDLF the transformation (50) from the characteristic limiter to the conservative limiter,

$$\begin{aligned}\Phi^{\mathrm{TVDLF}} &= \sum_k r^k(\phi^{\mathrm{LR}})^k = \sum_k r^k\alpha^k|a^{\max}| \\ &= R\cdot L\cdot\Delta U^{\mathrm{LR}}c^{\max}\frac{\Delta t}{\Delta x},\end{aligned} \tag{52}$$

simplifies to Eq. (39) since the R and L matrices cancel.

In the next subsection we complete our description of the TVD schemes by defining several versions of the slope limiters denoted by overlines in Eqs. (35)–(36) and (42)–(47).

3.7. *TVD Slope Limiters*

In the MUSCL schemes the ΔU differences of the conservative variables in Eq. (36), while in the non-MUSCL schemes the jumps in the characteristic variables $\alpha^k = l^k\cdot\Delta U$, or the expression $\alpha(|a| - a^2)$ in Eqs. (42)–(47) are limited by slope limiters. Denoting by w the quantity to be limited, any of the following limiters can be used.

$$\overline{w}_j = \mathrm{minmod}(w_{j-1/2}, w_{j+1/2}) \tag{53}$$

$$\overline{w}_j = \mathrm{minmod}(2w_{j-1/2}, 2w_{j+1/2}, \tfrac{1}{4}w_{j-1/2} + \tfrac{3}{4}w_{j+1/2}, \tfrac{3}{4}w_{j-1/2} + \tfrac{1}{4}w_{j+1/2}) \tag{54}$$

$$\overline{w}_j = \mathrm{minmod}(2w_{j-1/2}, 2w_{j+1/2}, \tfrac{1}{2}w_{j-1/2} + \tfrac{1}{2}w_{j+1/2}) \tag{55}$$

$$\overline{w}_j = s\max[0, \min(2|w_{j+1/2}|, sw_{j-1/2}), \min(|w_{j+1/2}|, 2sw_{j-1/2})], \tag{56}$$

where $s = \mathrm{sgn}(w_{j+1/2})$ and the generalized minmod function for $n > 1$ arguments is defined as

$$\begin{aligned}&\mathrm{minmod}(w_1, w_2, ..., w_n) = \mathrm{sgn}(w_1) \\ &\quad\max[0, \min(|w_1|, \mathrm{sgn}(w_1)w_2, ..., \mathrm{sgn}(w_1)w_n)].\end{aligned} \tag{57}$$

The limiters defined in Eqs. (53)–(56) will be referred to as *minmod*, *UMIST*, *Woodward*, and *superbee* limiters, respectively. Limiters which require small parameters to avoid division by zero are not listed. The minmod and the superbee limiters are the most and least diffusive of all acceptable symmetric two-variable limiters, respectively. The UMIST and Woodward limiters lie in between. The symmetric TVD scheme requires three-variable limiters, while the MUSCL TVD scheme may use weighted, asymmetric slope limiters (see Yee *et al.* [17]).

4. NUMERICAL TESTS

The numerical tests in this paper are all fully specified including discretisation, boundary conditions, adiabatic index etc. The tests are taken from the literature to allow comparison with previous work. They are selected on the basis of their simplicity (some of the more complicated tests were so loosely defined that we were unable to reproduce them even after considerable effort), their usefulness in terms of posing a real challenge to the algorithms, and their completeness; i.e., the tests together should cover most of the aspects of practical simulations.

Convection test problems serve as the most basic comparison for various numerical algorithms. We solve the continuity equation (1) with a prescribed constant velocity field. This is the simplest example of all hyperbolic equations; thus schemes giving unsatisfactory results should be abandoned. Convection tests have been published for several other algorithms which enable comparison of the results. The exact solution of the test problems, a shifted and unchanged initial density distribution, allows quantitative determination of the numerical accuracy. The error of a numerical solution will be defined as the average absolute error for the appropriate variable

$$E(U) = \frac{1}{N}\sum_{j=1}^{N}|U_j - U_j^{\mathrm{exact}}|. \tag{58}$$

In the one-dimensional HD and MHD test problems the full set of HD and MHD equations are solved with one spatial variable x. These systems of equations are nonlinear; thus the monotonicity of the numerical solutions is not guaranteed by a mathematical proof for any of the discussed algorithms and only numerical tests can reveal the properties of the schemes under various conditions.

Real applications are often multidimensional; thus the algorithms have to be tested in more than one dimension as well. Multidimensional MHD problems present a special challenge to schemes based on dimensionally split algorithms, namely the conservation of the divergence of the magnetic field. Often the errors associated with nonzero $\nabla\cdot\mathbf{B}$ are negligible, but other tests (like DeVore's current

carrying cylinder) indicate that there is a potential danger in not taking care of the numerically created magnetic monopoles.

In all cases the grid is uniform with cell centers at positions $x_1, ..., x_N$ in one dimension. Thus the computational region extends from $x_1 - \Delta x/2$ to $x_N + \Delta x/2$, where $\Delta x = x_{j+1} - x_j = \text{const}$. We shall usually define the computational region, which is independent of the resolution. A domain $x_L < x < x_R$ resolved by N grid cells corresponds to $x_j = x_L + (j - 1/2)(x_R - x_L)/N$ for $j = 1, ..., N$. All the initial conditions in the following subsections are defined in this discrete sense; thus x will represent the array $\{x_1, ..., x_N\}$.

Boundary conditions can be easily realized by introducing ghost cells at positions corresponding to x_0 and x_{N+1}, or even x_{-1} and x_{N+2}. The advantage of having two layers of ghost cells around the computational domain is that only the conservative variables have to be extrapolated to the boundaries and intermediate nonphysical quantities are determined the same way as inside the computational domain; the disadvantage is that one may not know the gradient of U outside the boundaries. In the test cases presented here the state of the ghost cells can always be easily determined. *Fixed*, *periodic*, *continuous*, and *reflective* boundaries will refer to keeping U fixed in the ghost cells, copying U from the periodically equivalent cells, copying the state from the closest cells of the computational domain, or mirroring the inside U with respect to the boundary and multiplying the normal momentum by -1, respectively. Boundaries are updated before each time step and for two-step methods after the half step as well. In dimensionally split two-step methods at the half step the boundaries in the actual direction need to be updated only. FCT requires boundary conditions for the transported and diffused U^d and U^D variables also. When not mentioned, continuous boundaries are taken.

4.1. *Convection of a Square Wave*

The square wave convection test problem was introduced by Boris and Book [9] for a basic comparison of various numerical algorithms. Although this test problem is very simple, it can cause numerical difficulties, like excessive numerical diffusion or unphysical oscillations, to some algorithms due to the presence of steep gradients.

We solve the continuity equation (1) on a one-dimensional uniform grid of $N = 100$ cells with $0 < x < 1$ and periodic boundary conditions. The velocity is $v_x = 1$ everywhere. The initial density profile contains a square wave,

$$\rho_j = \begin{cases} 2, & \text{if } 1 \le j \le 21, \\ 0.5, & \text{otherwise.} \end{cases} \tag{59}$$

Figure 1 shows the numerical solution and the average absolute errors with respect to the exact solution for different numerical schemes at time $t = 1.6$. For this simple equation the non-MUSCL TVD and TVDLF schemes are equivalent; thus the conclusions drawn for TVDLF apply to all TVD schemes. ETBFCT with CFL number 0.8 produces over- and undershoots since the monotonicity condition is violated (see Section 3.2). YDFCT and the TVD scheme with the superbee limiter are the most accurate; ETBFCT with $C = 0.4$ and TVD with the Woodward limiter follows; and, finally, TVD with the minmod limiter is the least accurate, due to its diffusivity.

4.2. *Convection of a Semicircle Wave*

The semicircle convection test problem was suggested by McDonald [18]. This test problem enables us to compare the phase errors of the algorithms.

Again a one-dimensional uniform grid of $N = 100$ cells is used with $0 < x < 1$ and periodic boundaries. Only the continuity equation (1) is solved with $v_x = 1$. The initial density field contains a 30-cell wide semicircle wave

$$\rho_j = \begin{cases} 1 + 2[1 - (j - 20)^2/15^2]^{1/2}, & \text{if } 5 < j < 35, \\ 1, & \text{otherwise.} \end{cases} \tag{60}$$

Results are compared at $t = 1.6$.

The numerical solutions and the respective errors for this test problem are shown in Fig. 2. Again, TVDLF represents all TVD schemes. YDFCT with its sixth-order phase error (for linear convection) is the most accurate and the TVD scheme with the Woodward limiter comes next. It is important to observe that the superbee limiter is too sharp; if the calculation is continued the semicircle will be distorted into a square wave. For this reason we shall abandon the superbee limiter for the rest of the paper although for certain applications, where discontinuities are of primary interest, it can be used successfully. The minmod limiter is rather diffusive; thus we shall not show results for it in the following tests unless some numerical instability occurs for the sharper limiters. For systems of equations, of course, different limiters for different quantities could be combined, but that would lead to many more combinations than we can present in this paper. Finally, we conclude that ETBFCT should be used with the Courant number $C < 0.5$ to avoid the undershoot behind the wave, although it is less prominent here (for $C = 0.8$) than behind the square wave, because the density gradient in the semicircle wave is less steep.

4.3. *Interaction of Two Blast Waves*

This HD test in one dimension was introduced by Woodward [14] to illustrate the strong relationship between the

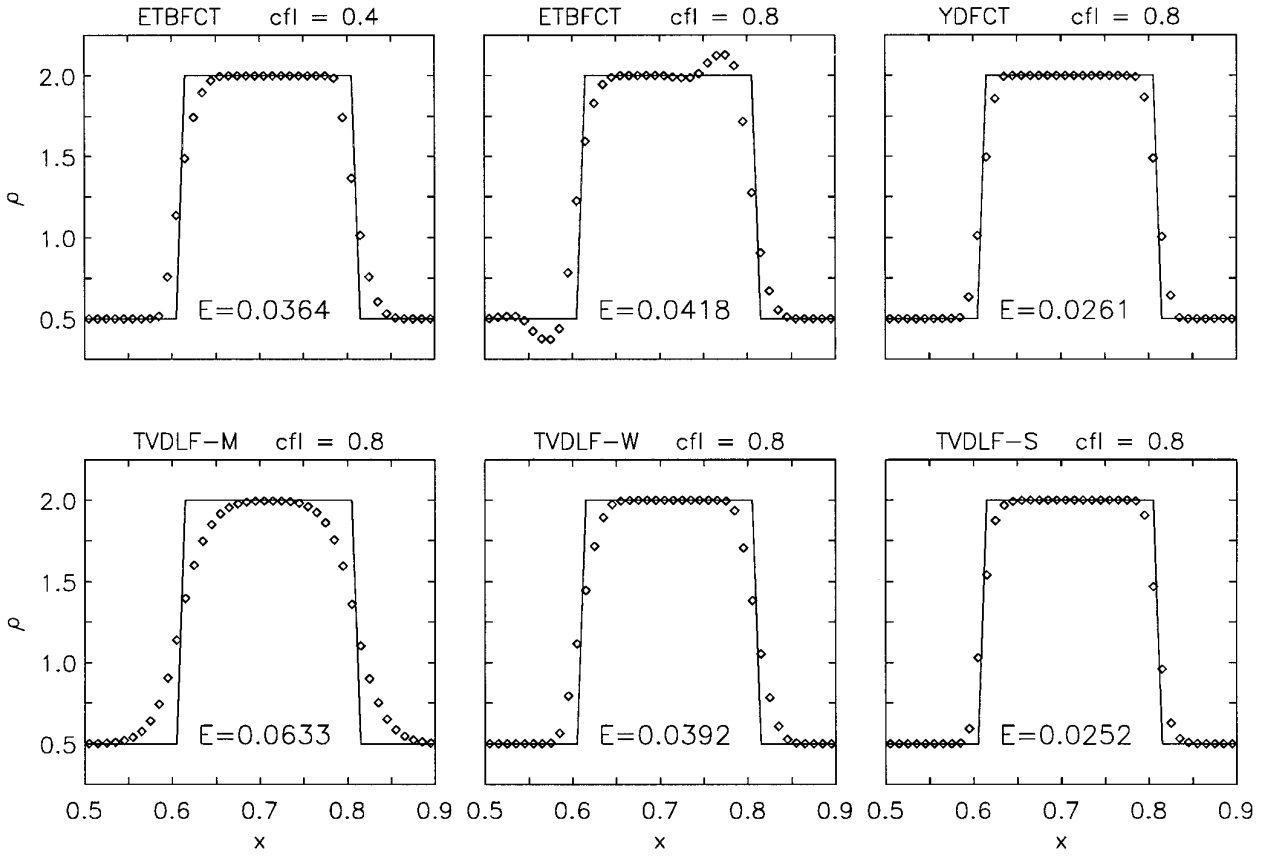

FIG. 1. Convection of a square wave. Density as a function of positions is shown at time $t = 1.6$. The Courant number and the method of computation is indicated at the top for each plot: the suffixes M, W, and S for the TVDLF scheme refer to the minmod, Woodward, and superbee limiters, respectively. The average absolute errors E with respect to the exact solution are shown within the plots.

accuracy of the overall flow solution and the thinness of discontinuities on the grid. It involves multiple interactions of strong shocks, rarefactions, and contact discontinuities with each other and with boundaries. The resulting hydrodynamic flow evolution is relatively complex and details are given by Woodward and Colella [14]. Because much of the important interactions take place in a small volume, this problem is very difficult to compute on a uniform Eulerian grid.

The boundaries are reflective on both sides. The initial conditions in terms of the primitive variables V are

$$V = \begin{cases} \rho = 1, v_x = 0, p = 1000, & \text{if } 0 < x < 0.1, \\ \rho = 1, v_x = 0, p = 0.01, & \text{if } 0.1 < x < 0.9, \\ \rho = 1, v_x = 0, p = 100, & \text{if } 0.9 < x < 1. \end{cases} \quad (61)$$

The adiabatic index is $\gamma = 1.4$. Calculations are performed on two different grids of $N = 200$ and $N = 1200$ points.

Figure 3 shows the distribution of ρ and v_x at time $t =$ 0.038. It is quite a sobering experience to see the relatively poor performance of the FCT and TVDLF schemes after their success with the simple convection tests. While the velocity is calculated quite accurately at the low resolution already (with some noise from FCT), the contact discontinuity at $x = 0.75$ in the density is in severe error for the low resolution FCT and TVDLF solutions and it is only qualitatively represented by TVD. Here the superiority of the characteristic based TVD scheme over TVDLF is quite clear. For $N = 1200$ grid points all methods converge to the same solution, but in the density ETBFCT has still some unphysical ripple, TVDLF is a bit diffused, and TVD comes closest to the "exact" solution (see PPM results by Woodward and Collela [14]) although the contact discontinuities are spread over many cells. Observe the slight oscillation at $x = 0.55$ produced by TVDLF; the monotonicity is not guaranteed for the nonlinear system of HD equations. Overall, the TVD/TVDLF schemes perform better than FCT for this test which involves the interaction of very strong hydrodynamical discontinuities.

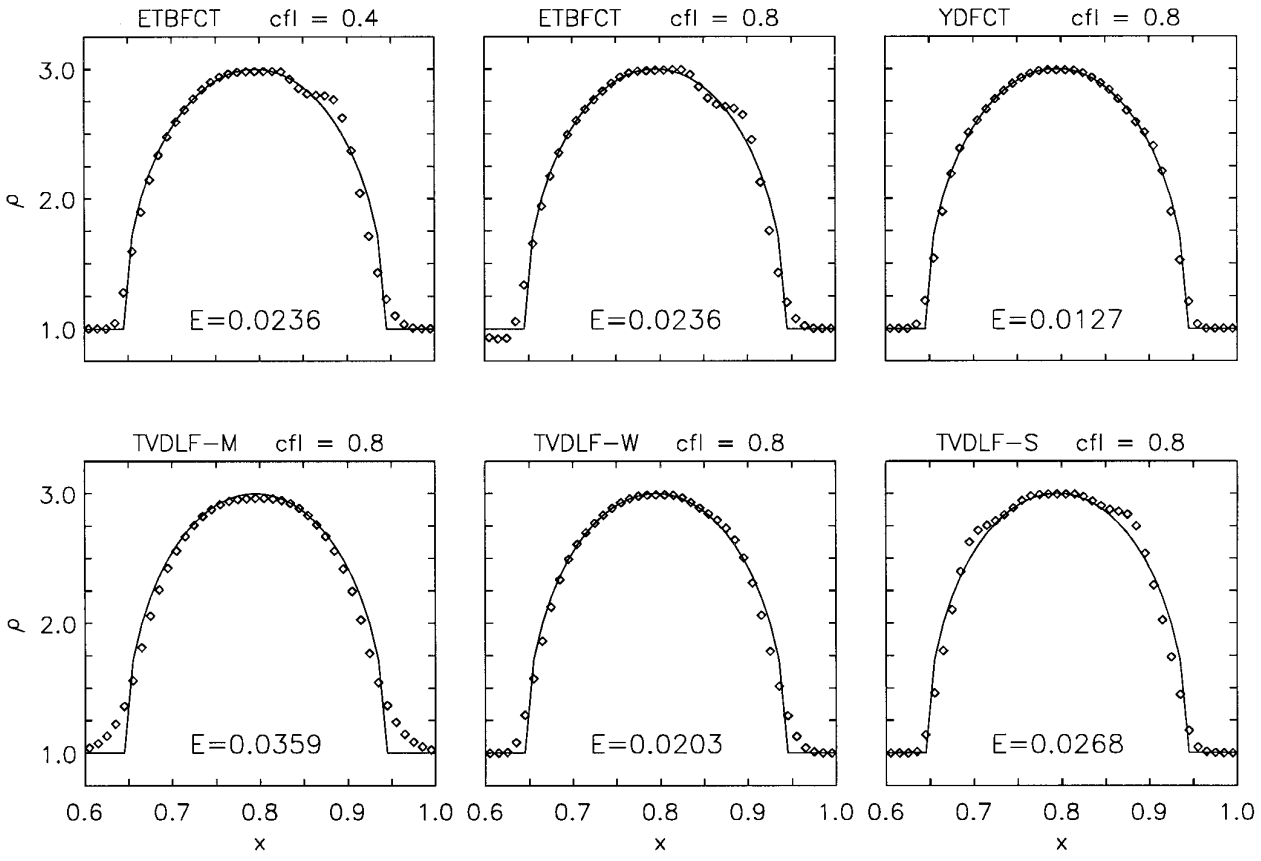

FIG. 2. Convection of a semicircle wave. Notation is the same as for Fig. 1.

4.4. *Strong Rarefaction Waves*

Einfeldt *et al.* [31] analyzed the one-dimensional hydrodynamic problem of two strong rarefaction waves moving symmetrically apart in opposite directions to illustrate certain failures of Godunov-type algorithms. The analytic solution produces vanishing pressure in the center, but the solution is not linearizable.

The initial conditions are

$$V = \begin{cases} \rho = 1, v_x = -2, p = 0.4, & \text{if } 0 < x < 0.5, \\ \rho = 1, v_x = +2, p = 0.4, & \text{if } 0.5 < x < 1, \end{cases} \tag{62}$$

and $\gamma = 1.4$. The calculation is stopped at $t = 0.1$ and $N = 100$ grid points are used.

Looking at Fig. 4 can convince us that none of the algorithms pass satisfactorily this difficult test. The FCT methods do not crash, but the density profiles are flattened instead of the correct U shape (see the figures in [31]). The TVDLF scheme passes with the minmod limiter and reduced time step ($C = 0.4$) only, and the results are hardly better than those of FCT. Finally, the linear Riemann solver of TVD fails unavoidably, and only artificial diffusion applied to the cells with negative pressure could make the code work. The diffusion coefficients could be tuned to get better results, but that problem-dependent approach is not in the spirit of modern shock-capturing schemes. A more satisfactory solution could be to use Einfeldt's positively conservative HLLE scheme, where necessary, as suggested by Quirk [32]. The test was of course designed to crash algorithms that can have undershoots in density and pressure, and in practical simulations such situations may occur rarely. It is, however, important to know how the algorithms work under such unfavorable conditions.

4.5. *Magnetic Shock Tube*

This test problem by Brio and Wu [33] became a benchmark for magnetohydrodynamic codes. It produces a fast rarefaction fan and a slow compound wave (consisting of a slow rarefaction wave attached to a slow shock plus a rotational discontinuity; alternatively, the two discontinuities can be interpreted as an intermediate shock) moving to the left, and a contact discontinuity, a slow shock, and a fast rarefaction fan moving to the right. The one-dimen-

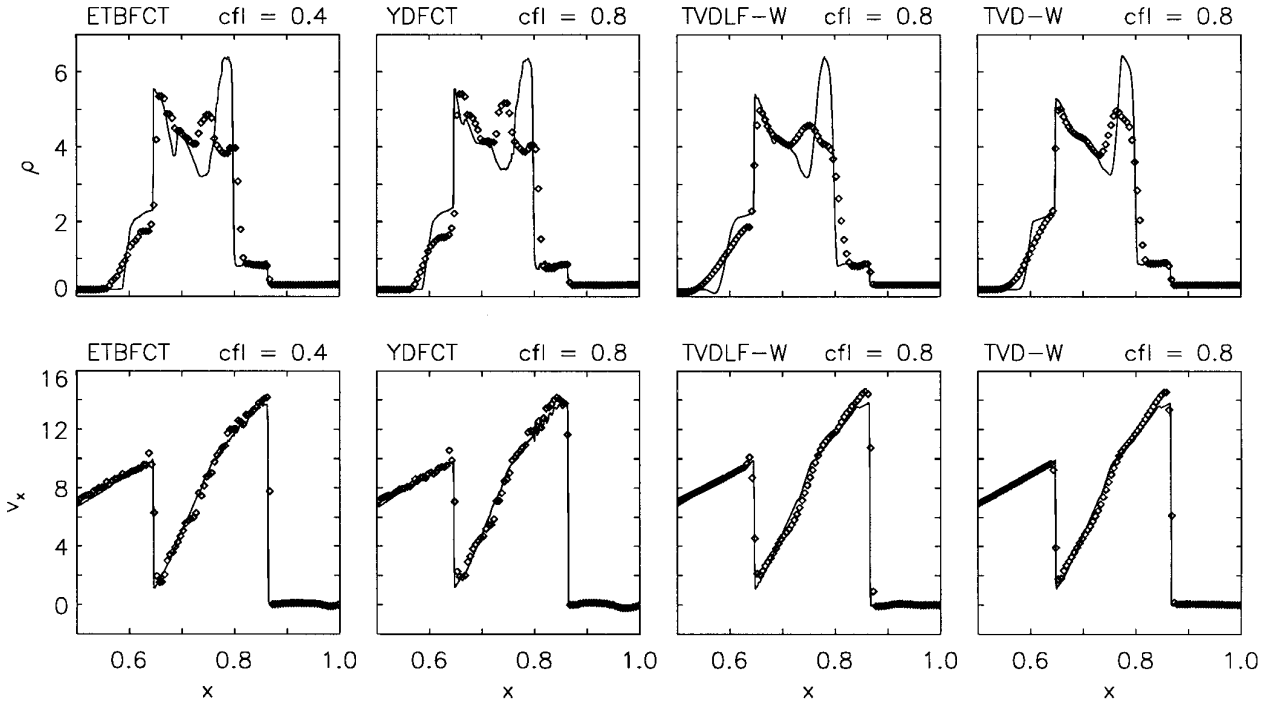

FIG. 3. Two interacting blast waves. The density (top) and velocity (bottom) are shown at $t = 0.038$. Calculations were performed on grids with 200 (symbols) and 1200 (solid line) points.

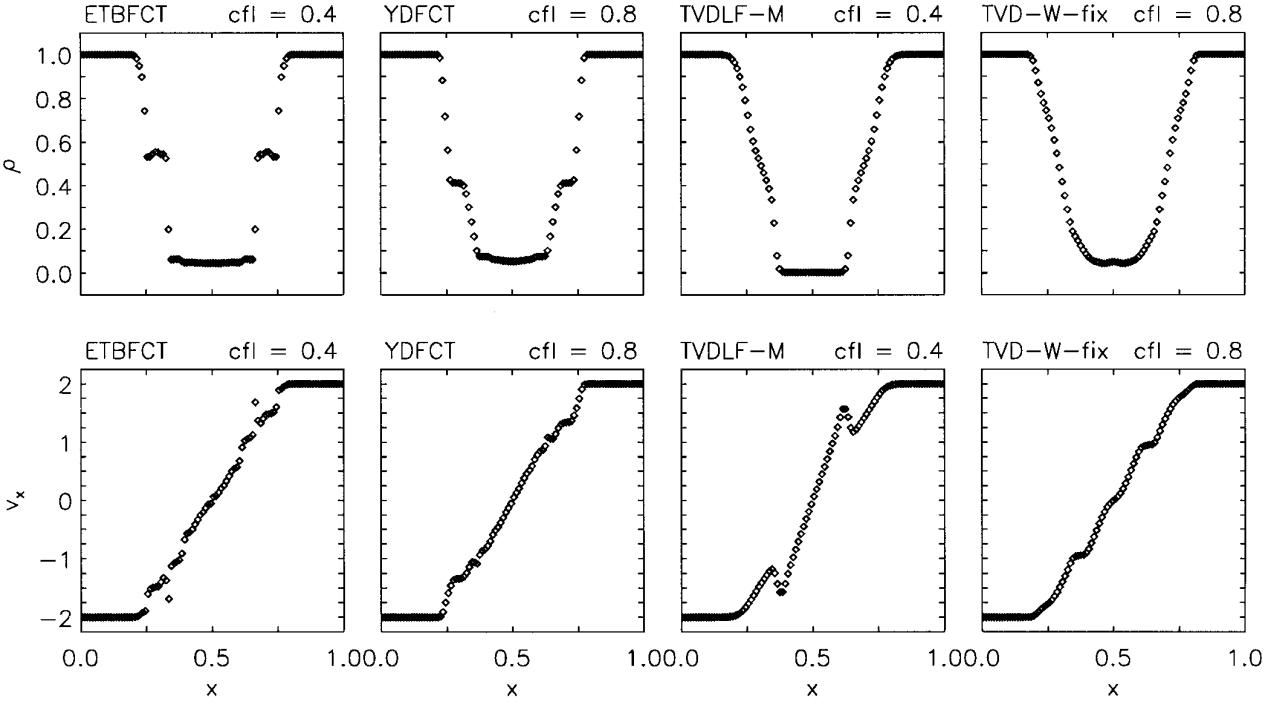

FIG. 4. Strong rarefaction waves. The density (top) and velocity (bottom) is shown at $t = 0.1$. TVDLF was run with the minmod limiter and with half the maximum time step, while the non-MUSCL TVD scheme required a fix against negative pressures (see discussion in the text).

sional MHD equations are solved with two vector components for **v** and **B**; i.e., v_z and B_z are taken to be zero.

The initial conditions are

$$V = \begin{cases} \rho = 1, \quad \mathbf{v} = 0, p = 1, \quad B_x = 0.75, B_y = +1, \\ \qquad\qquad\qquad\qquad\qquad \text{if } 0 < x < 0.5, \\ \rho = 0.125, \mathbf{v} = 0, p = 0.1, B_x = 0.75, B_y = -1, \\ \qquad\qquad\qquad\qquad\qquad \text{if } 0.5 < x < 1, \end{cases} \tag{63}$$

and $\gamma = 2$. Results are compared at $t = 0.1$ for coarse ($N = 200$) and fine ($N = 800$) grids.

We plotted ρ and v_x for the different numerical solutions in Fig. 5. The numerical errors in other variables show similar effects. The low resolution results show a distinct advantage of the smooth TVD solutions over the spurious oscillations of FCT. At high resolution YDFCT seems to be somewhat better than ETBFCT and comparable to TVDLF, which has a spurious undershoot in velocity at $x = 0.8$ and a contact discontinuity spreading over 10 cells at $x = 0.6$. Not surprisingly the characteristeric-based TVD scheme is superior in every respect. The difference is most significant on the $N = 200$ grid.

4.6. *Propagation of Shear Alfvén Waves*

This simple one-dimensional test problem was described by Stone and Norman [34] to illustrate that some schemes that perform quite well for hydrodynamical tests may have difficulties with the propagation of Alfvén waves. The initial transverse velocity pertubation produces two linearly polarized Alfvén waves moving in opposite directions.

The grid has $N = 150$ cells in the $0 < x < 3$ computational region. Again only the x and y components of **v** and **B** are considered, although using circularly polarized Alfvén waves with three components could serve as an even better test, since those waves are exact solutions of the MHD equations for arbitrary amplitudes. Initially the magnetic field is longitudinal, and there is a slight transverse velocity perturbation in the middle third of the mesh,

$$V = \begin{cases} \rho = 1, v_x = 0, v_y = 0.001, B_x = 1, B_y = 0, p = 10^{-9}, \\ \qquad\qquad\qquad\qquad\qquad \text{if } 1 < x < 2, \\ \rho = 1, v_x = 0, v_y = 0, \qquad B_x = 1, B_y = 0, p = 10^{-9}, \\ \qquad\qquad\qquad\qquad\qquad \text{otherwise}, \end{cases} \tag{64}$$

and $\gamma = 1.4$. The calculation is stopped at $t = 0.8$ and $N = 150$ grid points are used.

Inspecting Fig. 6 shows that in this test ETBFCT is more accurate than YDFCT, but the TVD schemes are superior to both. TVDLF has very small under- and overshoots in velocity, but otherwise it is as sharp as the Riemann solver-based TVD method. When the time step is reduced to $C = 0.4$, YDFCT produces comparable results to ETBFCT. We also note that due to the very small thermal pressure, roundoff errors may create difficulties in the Riemann solver unless the analytical inequalities among the fast, slow, and Alfvén speeds are enforced numerically.

4.7. *Double Mach Reflection of a Strong Shock*

This test by Woodward and Colella [14] became a reference problem for two-dimensional shock hydrodynamics. A planar shock is reflected from a wedge at a 60° angle and a self-similar flow develops. The most complicated structures, including two Mach stems with two contact discontinuities, form in the rather small region beyond the reflection of the incident shock. The first Mach shock is strong and it connects the leading triple point with the reflecting wall. The second Mach shock which extends from the trailing triple point is rather weak and it vanishes entirely at the point it would reach the contact discontinuity from the first Mach reflection. Where the first contact discontinuity approaches the reflecting wall, the flow of the denser fluid is deflected by a pressure gradient buildup in the region. The result is that a jet of the denser fluid is formed which propagates to the right along the wall. The second contact discontinuity is extremly weak.

The problem is set up using a rectangular domain, one unit high and four units long, i.e., $0 < x < 4$ and $0 < y < 1$. The left boundary and the lower boundary from $x = 0$ to $\frac{1}{6}$ are always set to the postshock conditions. The lower boundary is reflecting for $\frac{1}{6} < x < 4$, while the right boundary is continuous and the upper boundary is time dependent following the exact motion of the shock wave; i.e., the boundary cells are set to ambient values for $x_j = x_s(t)$ and the postshock values for $x_j \le x_s(t)$, where $x_s(t)$ is the position of the shock at time t. The planar shock is initially at a 60° angle to the x-axis, starting at $x = \frac{1}{6}$ at the bottom and extending to the top of the grid, propagating at a speed of 10. Thus it intersects the upper boundary at $x_s(t) = 10t/\sin 60° + 1/6 + 1/\tan 60°$. The pre- and postshock conditions are

$$V = \begin{cases} \rho = 1.4, v_x = 0, v_y = 0, p = 1, \text{if } x < \frac{1}{6} + y/\tan 60° \\ \rho = 8, v_x = 8.25 \sin 60°, v_y = -8.25 \cos 60°, p = 116.5, \\ \qquad\qquad\qquad\qquad\qquad \text{otherwise} \end{cases} \tag{65}$$

With the adiabatic index $\gamma = 1.4$ the preshock sound speed is 1; thus the Mach number is 10. The calculation is stopped at $t = 0.2$.

Density contour plots are presented in Fig. 7 for coarse

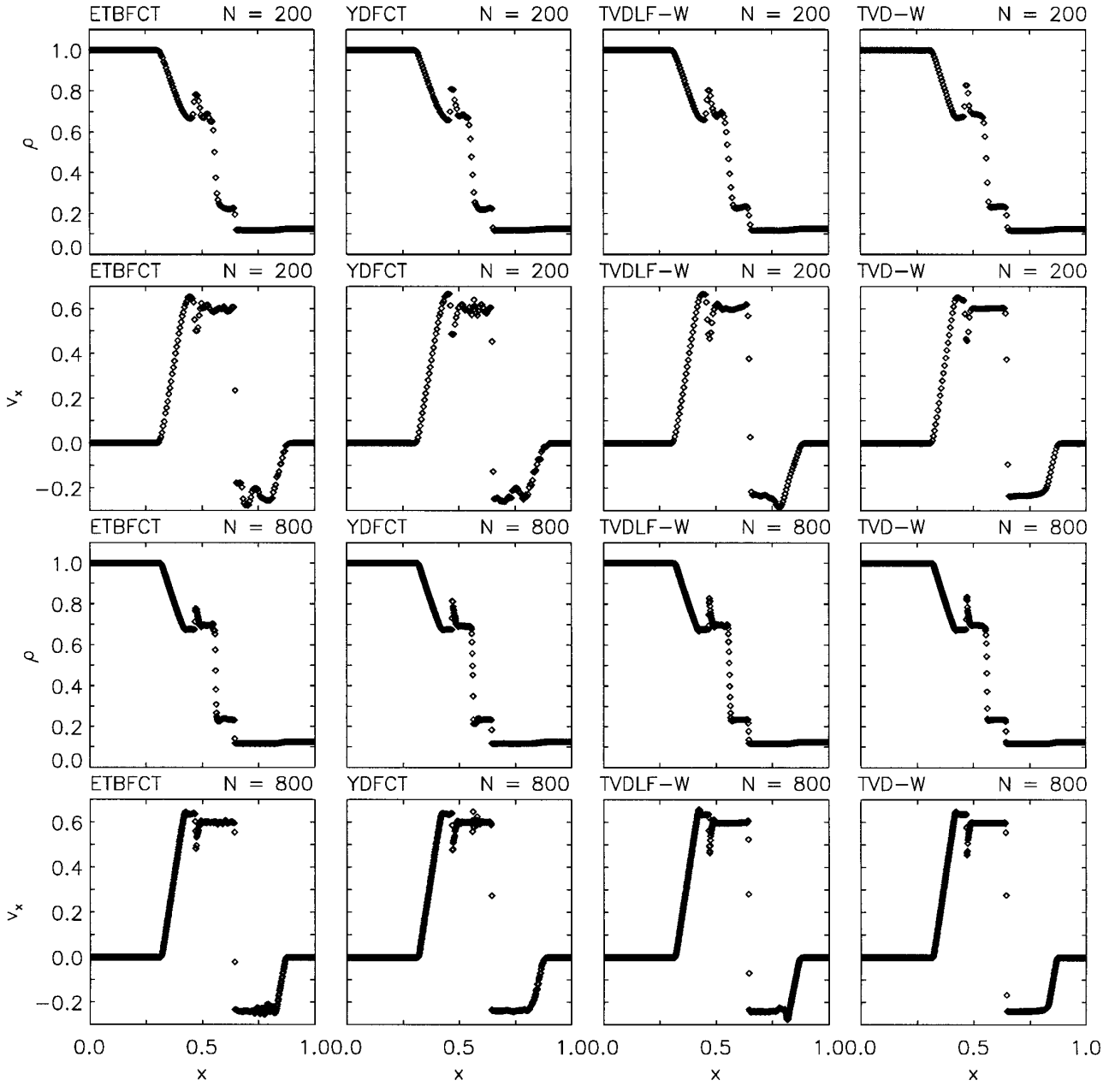

FIG. 5. Magnetic shock tube. Density (first and third rows) and the longitudinal velocity (second and fourth rows) are shown at time $t = 0.1$. Calculations were performed on a low resolution grid with $N = 200$ (upper half), and on a high resolution grid with $N = 800$ (lower half) cells.

(120×30) and fine (480×120) grids, but only the $x < 3$ parts are shown. For both resolutions FCT produces thinner shocks (although staircased on the coarse grid), but it also generates more noise behind the shock fronts than the TVD schemes. The contact discontinuity from the leading Mach shock is kinked near the triple point in the low resolution FCT solutions. At high resolution all methods show the essential structures, although the jet at the lower boundary is not very well defined, except for the non-MUSCL TVD scheme. Note, however, a small perturbation in the first Mach shock just in front of the mushroom-shaped head of the jet. For the Woodward limiter the entropy fix (48) eliminates most of this error, but if a superbee limiter was used for the contact discontinuities, as proposed by Yee [11], the error would be much more pronounced and the entropy fix seems to be unable to cope with the problem. Other entropy fixes or other versions of the TVD scheme may behave differently, but in general

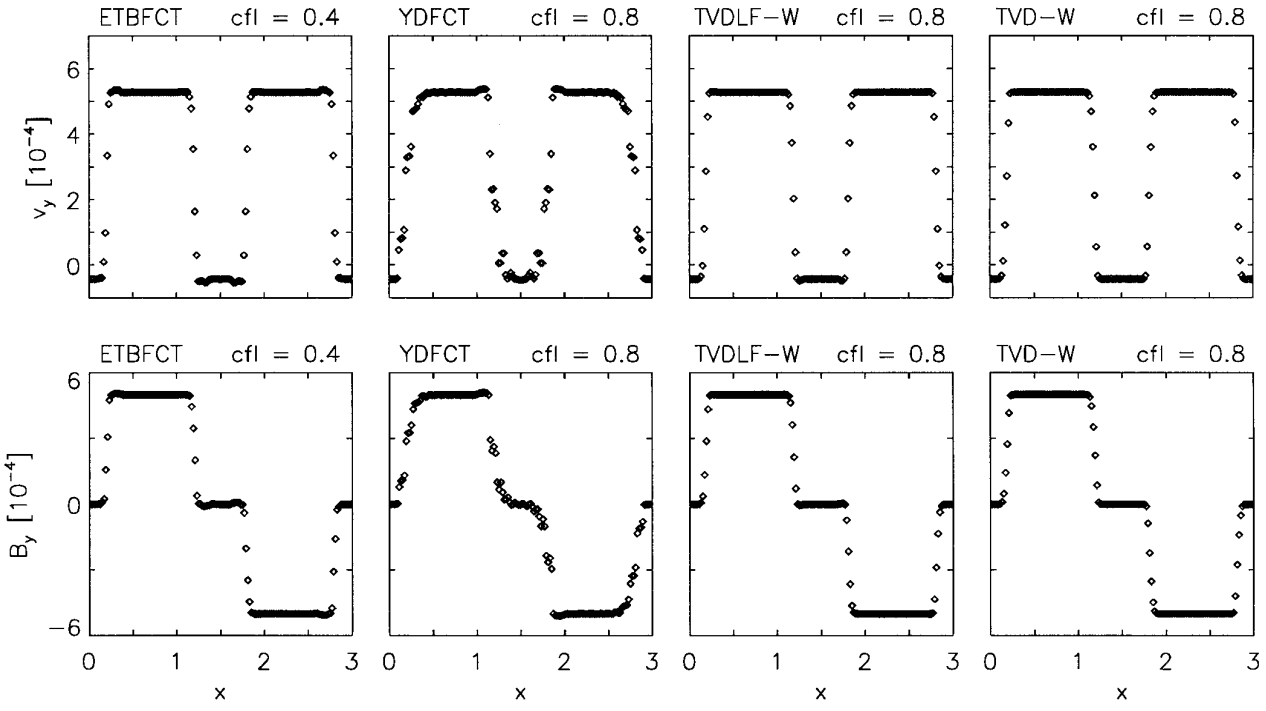

FIG. 6. Propagation of shear Alfvén waves. Transverse velocity (top) and transverse magnetic field (bottom) are plotted at $t = 0.8$. If the Courant number is reduced to 0.4, YDFCT produces results comparable with ETBFCT.

one should check the results gained with sharp limiters against some entropy conserving scheme.

4.8. *Advection of a Current-Carrying Cylinder*

DeVore [21] used this test to demonstrate the performance of his divergence **B** conserving fully multidimensional FCT algorithm using a staggered grid. Only the induction equation (4) is solved; the rest of the flow variables are kept constant. An off-center placed current-carrying cylinder orbits around the center of the grid in a counterclockwise direction. There is a sheath of return current on the surface of the cylinder. The circular advection of the cylinder is an exact solution of the induction equation.

The calculations are performed on a 100×100 mesh, and the computational domain is $-50 < x, y < 50$. The cylinder is initially centered in the upper half-plane and its radius is set to $R = 15$. The angular speed of the rotation around the center of the grid is 1; thus

$$V = \begin{cases} v_x = -y, v_y = x, A_z = R/2 - [x^2 + (y-25)^2]/(2R), \\ \qquad \text{if } x^2 + (y-25)^2 < R^2, \\ v_x = -y, v_y = x, A_z = 0, \\ \qquad \text{otherwise.} \end{cases} \tag{66}$$

The magnetic field components are obtained by discrete central differencing the vector potential, $B_x = \Delta A_z/\Delta y$ and $B_y = -\Delta A_z/\Delta x$. This definition ensures $\nabla \cdot \mathbf{B} = 0$ exactly for the initial condition. The calculation is stopped after a full rotation around the center after 1256 time steps, where a fixed time step $\Delta t = 0.005$ is used. The only difference from DeVore's test problem is in the spatial discretization since he used a staggered grid, while we use cell-centered quantities for the discrete representation of the magnetic field.

We found that it is necessary to use Powell's corrective term in Eq. (4) for all the numerical schemes to obtain acceptable results. We also note that the diffusion and antidiffusion steps of FCT have to be applied for both the x and y sweeps for both components of the magnetic field, even though the transport fluxes $f = v_x B_x$ and $f = v_y B_y$ in Eq. (4) are cancelled by identical source terms on the right-hand side. In FCT, however, the transport flux and the source terms are discretized differently, thus the cancellation in multidimensional simulations is not exact.

We plot the current density $J = \nabla \times \mathbf{B}$ and the magnitude of the magnetic field $B = |\mathbf{B}|$ for the initial data and the final results in Fig. 8. The relative errors, following DeVore's definition,

$$E(B) = \frac{\sum_{i,j=1}^{N} |B_{i,j} - B_{i,j}^{\text{exact}}|}{\sum_{i,j=1}^{N} |B_{i,j}^{\text{exact}}|}, \tag{67}$$

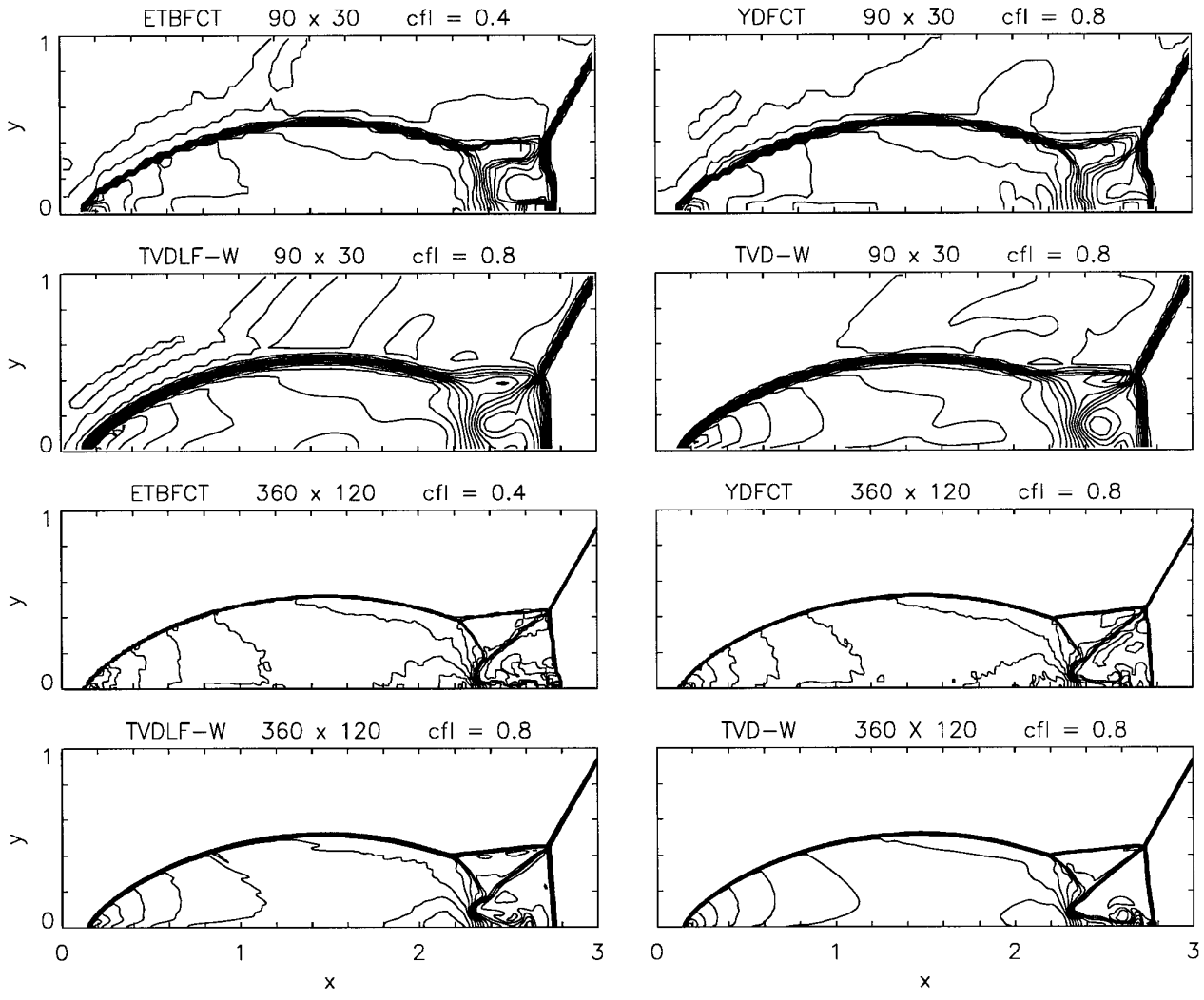

FIG. 7. Double Mach reflection of a strong shock. The density is plotted at $t = 0.2$ with 30 contour levels from minimum to maximum values. The calculations were performed on 120×30 (upper half) and 480×120 grids, but only the $x < 3$ portions are shown.

and a similar expression for $E(J)$, are also indicated on the plots. ETBFCT provided the smallest error, YDFCT and TVDLF are similar, while the non-MUSCL TVD scheme is the least accurate. The probable explanation for such a poor performance from the usually most accurate TVD scheme is that here we solve the induction equation only, while the Riemann solver uses the characteristics for the full set of MHD equations. There seems to be little interest in writing a Riemann solver just for this test problem; on the other hand, the FCT and TVDLF algorithms work optimally without modification.

For comparison DeVore obtained $E(B) = 0.25$ and $E(J) = 0.79$ with his staggered grid FCT scheme. We cannot compare the accuracy for the vector potential, since $\nabla \cdot \mathbf{B}$ is not zero due to the numerical errors and the vector potential is not well defined.

4.9. *MHD Vortex*

Orszag and Tang [35] constructed this simple model to study the evolution of MHD turbulence. It was generalized by Dahlburg and Picone [36] for the case of a fully compressible medium and used as a numerical test by Zachary *et al.* [8]. The initial conditions are superpositions of periodic sine waves containing X-points in both the velocity and magnetic fields, but with different wave lengths. The flow becomes very complex, as expected, from a transition toward turbulence.

The grid is 192×192 large with $0 < x, y < 2\pi$ and periodic boundary conditions. The initial vortex structure is defined by

$$\begin{aligned} &\rho = 25/9, \quad v_x = -\sin y, \quad v_y = \sin x, \\ &B_x = -\sin y, \quad B_y = \sin 2x, \quad p = 5/3, \end{aligned} \tag{68}$$

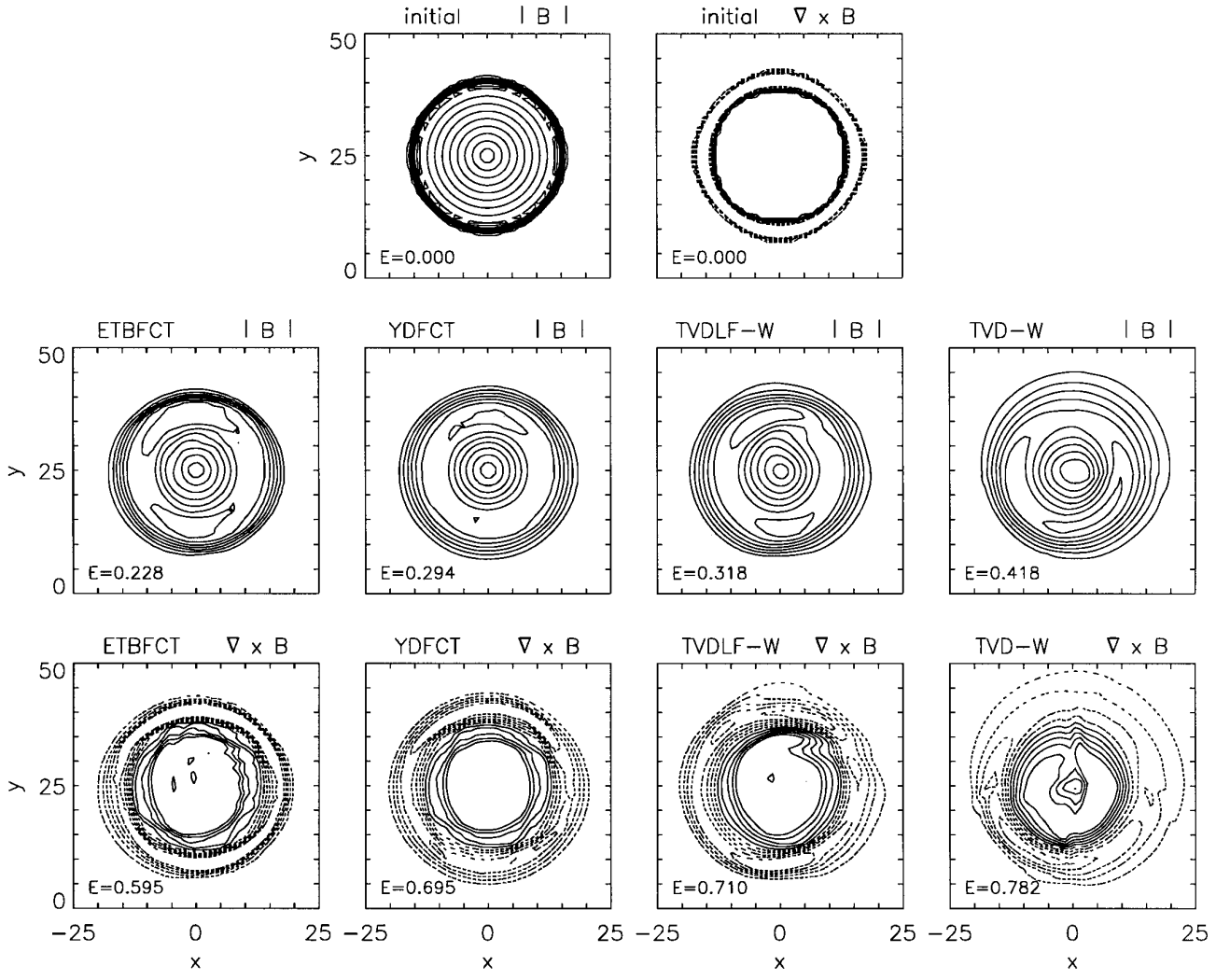

FIG. 8. Advection of a current-carrying cylinder. The initial conditions (top) and the advected results at time $t = 6.28$ for the magnitude of the magnetic field $|\mathbf{B}|$ (middle) and for the current density $J = \nabla \times \mathbf{B}$ (bottom) are plotted. Only one quarter of the full grid centered on the cylinder is shown. The contour levels for $|\mathbf{B}|$ are 0.1, 0.2, ..., 0.9, and for J they are $-0.9J_0$, $-0.7J_0$, ..., $0.7J_0$, $0.9J_{90}$, where $J_0 = 2/15$ is the initial current density *inside* the cylinder. The negative levels for the current density are drawn with dashed contours. The average relative errors E with respect to the exact solutions for $|B|$ and J are indicated within the plots. The return current on the surface of the cylinder (initially one cell wide) cannot be correctly advected by any of the methods, the contour lines inside the cylinder and the distortions are of greater significance.

and $\gamma = \frac{5}{3}$. All numbers are truncated to six decimal places for the initial conditions, but the calculations are performed in double precision.

Figure 9 shows contour levels for the thermal pressure p after 300 time steps (600 for ETBFCT) corresponding to approximately $t = 3.1$. It is quite reassuring to see that all methods give similar results. For the non-MUSCL TVD scheme it is necessary to make use of Powell's [29] eight-wave Riemann solver with the source terms proportional to $\nabla \cdot \mathbf{B}$. Without the source terms the code crashed, except with the minmod limiter. For the TVDLF scheme including Powell's source terms made little difference, but it improved the FCT results significantly. Although the source terms are not in a conservation form, the total momentum, magnetic flux and energy seems to be conserved to a high accuracy. This may be due to the symmetry of the problem or due to the fact that the corrections are small and on average they tend to cancel each other.

5. CONCLUSIONS

This paper is devoted to the comparison of various numerical methods for simulations of hydrodynamic and magnetohydrodynamic problems. ETBFCT is used by many researchers, it offers stability and sharp resolution for a relatively small effort in coding. It can be easily

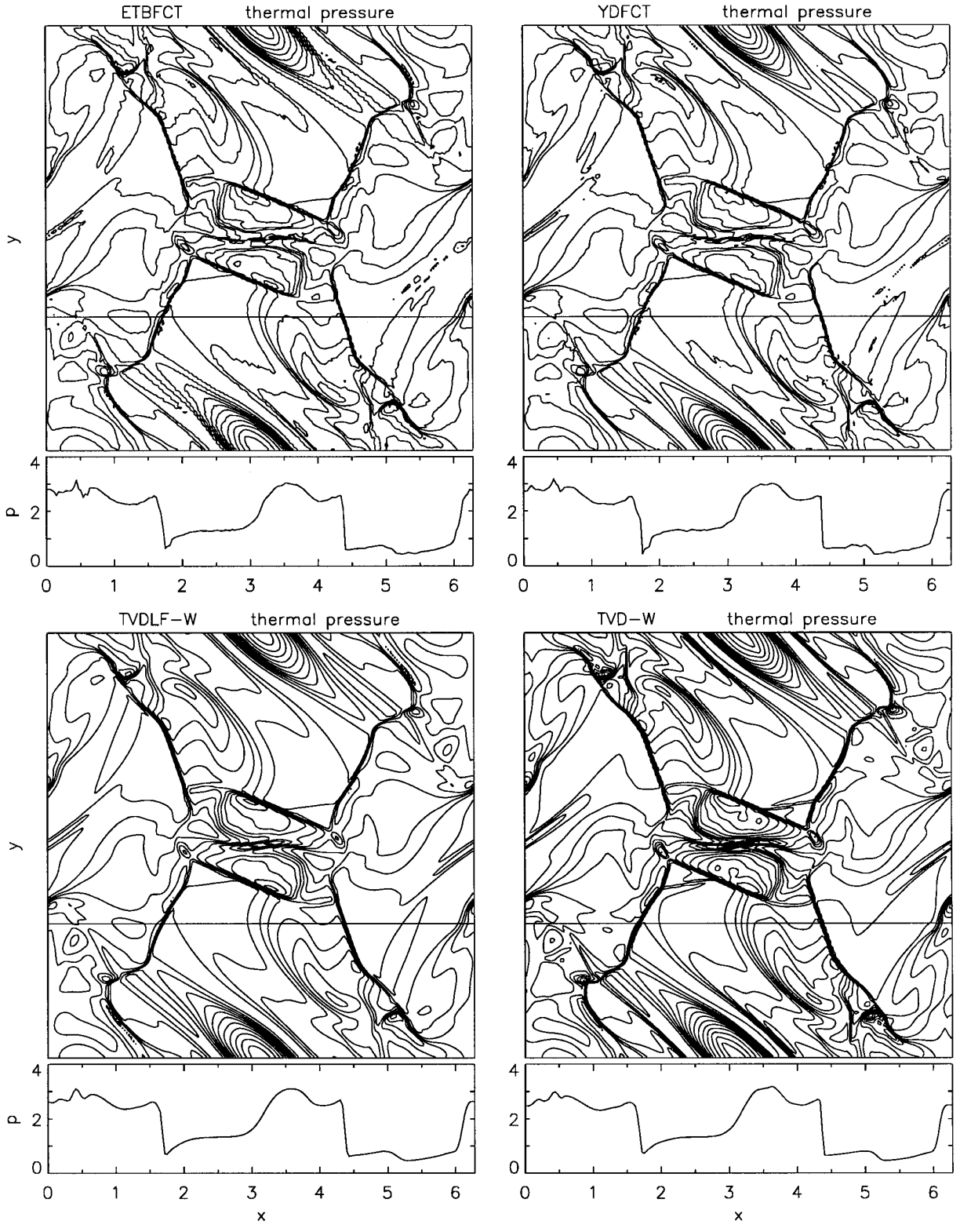

FIG. 9. Orszag–Tang vortex system. The thermal pressure is plotted with 15 contour levels after 300 time steps (600 for ETBFCT) corresponding to approximately $t = 3.1$. A cut at the 60th row of cells (at $y_{60} = 1.9471$ as indicated by a horizontal line) is shown below each contour plot. Results are to be compared with the figure in [8].

TABLE I

Comparison of Performance and Some Features

Tests/Features	ETBFCT	YDFCT	TVDLF	TVD
1. Square wave	8	9	8	8
2. Semicircle wave	7	10	9	9
3. Blast waves	5	5	6	7
4. Rarefaction waves	2	2	2	2
5. MHD shock tube	6	7	8	10
6. Alfvén waves	7	6	9	10
7. Mach reflection	7	7	7	9
8. Current cylinder	7	6	6	5
9. MHD vortex	7	7	8	9
Relative speed	4	8	10	7
Independent of eqs.	+	+	+	−
Simple to code	+	+	+	−
Unsplit dimensions	+	−	−	+
Implicit version	−	−	−	+

modified to YDFCT to speed up calculations and to improve accuracy in some cases. Note, however, that YDFCT is restricted to a dimensionally split implementation, while ETBFCT can be made fully multidimensional. TVDLF is not more complicated to code than the FCT algorithms, and while it may be a bit more diffusive, often the smoothness of the solution more than compensates for that. It may be best used in combination with FCT; the discontinuities are usually sharply resolved by the flux-corrected transport schemes, while the spurious oscillations can be identified when a comparison is made with the solution by the high order Lax–Friedrichs method. Another advantage of the TVDLF algorithm is that it can be *relatively* easily upgraded to the more advanced Riemann solver-based MUSCL TVD scheme. Note, however, that the Riemann solver corresponds to a specific system of equations, and when the equations are changed, a new Riemann solver has to be implemented. This is a rather cumbersome task, especially for the MHD equations.

While Riemann solvers usually produce sharp and monotonic profiles, they are prone to various errors (e.g., Quirk [32], Roberts, [37]). The need for entropy fixes, switches to other methods, rarefaction-recognizing algorithms is rather typical. It is therefore useful to have some simpler methods available for comparison, both in the development and in the production stages. Convergence tests on finer and finer meshes are sometimes prohibited by the limited computational resources; in that case results by two or three different algorithms for the same initial data can be a valuable source of information. Such comparisons may lead to better founded conclusions for new simulations when we do not know the physical solution in advance.

In Table I we summarize our experience with the four methods tested: ETBFCT with CFL condition $C = 0.4$, YDFCT with $C = 0.8$, and TVDLF and the non-MUSCL TVD schemes with the Woodward limiter and $C = 0.8$. The scores on the 1 to 10 scale, with 10 being the best and 1 complete failure, are subjective, but express our overall impression. The relative computational speed and the other features listed at the end of the table highlight some differences that cannot be seen in the plots of the test results.

The occasional failures of some or all of the methods described in this paper show the directions for further development. We found that Powell's source terms proportional to $\nabla \cdot \mathbf{B}$ improve the results for multidimensional MHD simulations for all the investigated methods. Although the source terms are not in a conservation form, and the error in $\nabla \cdot \mathbf{B}$ is not eliminated by them, in the two multidimensional MHD test cases studied here, and in all other tests tried by the authors, the errors remained small. Conserving $\nabla \cdot \mathbf{B}$ to a high accuracy may be crucial for certain applications. The simplest remedy may be the use of a projection scheme (Brackbill and Barnes [38]) to remove the numerically generated divergence of the magnetic field after each step. One may also use the vector potential as a variable with some spatially third-order TVD method. Positivity of pressure and density may be ensured by switching to some positively conservative scheme, like HLLE, where necessary, or one may try to use non-linear Riemann solvers to overcome these difficulties. These modifications and improvements are subjects of future work.

ACKNOWLEDGMENTS

G. Tóth received partial support from the Hungarian Science Foundation, Grant F017313. D. Odstrčil acknowledges support provided by the Academy of Sciences of the Czech Republic Grant 303402, the ESO-CEEE Programme Grant B-05-048, and the Leids Kerkhoven–Bosscha Fonds. He thanks the kind hospitality of the Sterrenkundig Instituut of Utrecht University.

REFERENCES

1. C. Hirsch, *Numerical Computation of Internal and External Flows* (Wiley, New York, 1990).
2. R. J. LeVeque, *Numerical Methods for Conservation Laws* (Birkhäuser, Basel, 1992).
3. C. A. J. Fletcher, *Computational Techniques for Fluid Dynamics* (Springer, Berlin, 1991).
4. D. Ryu and T. W. Jones, *Astrophys. J.* **442,** 228 (1995).
5. D. Ryu, T. W. Jones, and A. Frank, *Astrophys. J.* **452,** 785 (1995).
6. D. Balsara, P. L. Roe, and K. G. Powell, preprint.
7. W. Dai and P. R. Woodward, *J. Comput. Phys.* **111,** 354 (1994).
8. A. L. Zachary, A. Malagoli, and P. Colella, *SIAM J. Sci. Comput.* **15,** 263 (1994).
9. J. P. Boris and D. L. Book, *J. Comput. Phys.* **11,** 38 (1973).
10. A. Harten, *J. Comput. Phys.* **49,** 357 (1983).
11. H. C. Yee, NASA TM-101088, 1989 (unpublished).

12. B. Cockburn, S.-Y. Lin, and C.-W. Shu, *J. Comput. Phys.* **84,** 90 (1989).
13. A. A. Barmin, A. G. Kulickovskiy, and N. V. Pogorelov, *J. Comput. Phys.* **126,** 77 (1966).
14. P. R. Woodward and P. Colella, *J. Comput. Phys.* **54,** 115 (1984).
15. J. M. Stone, J. F. Hawley, C. R. Evans, and M. L. Norman, *Astrophys. J.* **388,** 415 (1992).
16. J. P. Boris, NRL *Memorandum Report 3237* (NRL, Washington, DC 1976).
17. H. C. Yee, G. H. Klopfer, and J.-L. Montagné, *J. Comput. Phys.* **88,** 31 (1990).
18. E. S. Oran and J. P. Boris, *Numerical Simulation of Reactive Flow* (Elsevier, New York, 1987), p. 296.
19. J. C. T. Wang and G. F. Widhopf, *J. Comput. Phys.* **84,** 145 (1989).
20. S. T. Zalesak, *J. Comput. Phys.* **31,** 335 (1979).
21. C. R. DeVore, *J. Comput. Phys.* **92,** 142 (1991).
22. G. Strang, *SIAM J. Numer. Anal.* **5,** 506 (1968).
23. D. Odstrčil, *J. Comput. Phys.* **91,** 71 (1990).
24. D. Odstrčil, *J. Comput. Phys.* **108,** 218 (1993).
25. P. L. Roe, *J. Comput. Phys.* **43,** 357 (1981).
26. G. Tóth, ''A General Code for Modeling MHD Flows on Parallel Computers: Versatile Advection Code,'' in *Proceedings, Int. Astron. Union Colloqium 153, Makuhari, Japan, May 22–26, 1995.*
27. G. Tóth, ''A General Code for Modeling MHD Flows on Parallel Computers: Versatile Advection Code,'' in *Astrophys. Lett. & Comm., Proceedings, NATO Advanced Study Institute on Solar and Astrophysical Magnetohydrodynamic Flows, Phodele Beach, Crete, June 12–22, 1995.*
28. P. L. Roe and Balsara, *SIAM J. Appl. Math.*, **56**, 57 (1996).
29. K. G. Powell, ICASE *Report No. 94–24, Langley, VA,* 1994 (unpublished).
30. T. I. Gombosi, K. G. Powell, and D. L. De Zeeuw, *J. Geophys. Res.* **99,** 21,525 (1994).
31. B. Einfeldt, C. D. Munz, P. L. Roe, and B. Sjögreen, *J. Comput. Phys.* **92,** 273 (1991).
32. J. J. Quirk, *Int. J. Numer. Methods Fluids* **18,** 555 (1994).
33. M. Brio and C. C. Wu, *J. Comput. Phys.* **75,** 400 (1988).
34. J. M. Stone and M. L. Norman, *Astrophys. J. Suppl.* **80,** 791 (1992).
35. A. Orszag and C. M. Tang, *J. Fluid Mech.* **90,** 129 (1979).
36. J. M. Picone and R. B. Dahlburg, *Phys. Fluids B* **3,** 29 (1991).
37. T. W. Roberts, *J. Comput. Phys.* **90,** 141 (1990).
38. J. U. Brackbill and D. C. Barnes, *J. Comput. Phys.* **35,** 426 (1980).